Graphical Abstract

Vortex Shape Morphology Controls Resonant Fatigue Failure Mode: An Analytical Framework Linking Draft Tube Flow Physics to Blade Life Prediction in Francis Turbines

Jiaxuan Jiang, Bohhaoi Kuai

Highlights

Vortex Rope Morphology Controls Resonance Fatigue Failure Mode: An Analytical Framework Linking Draft Tube Flow Physics to Blade Life Prediction in Francis Turbines

Jiaxun Jiang, Reshmi Rosa

- Different vortex rope morphologies excite different runner vibration modes
- Helical, columnar, and double-helix ropes concentrate stress at distinct blade locations
- Operating condition determines fatigue failure mode, not merely failure rate
- One-way FSI is justified: blade deformations are five orders of magnitude below draft tube scales
- Condition monitoring must track pressure phase distribution, not only amplitude

Vortex Rope Morphology Controls Runner Fatigue Failure Mode: An Analytical Framework Linking Draft Tube Flow Physics to Blade Life Prediction in Francis Turbines

James Jung[1,*], Bozhao Rui[1]

[1]Department of Engineering Science, University of Oxford, Parks Road, Oxford, OX1 3PJ, United Kingdom

Abstract

Francis turbines operating off-design develop distinct draft tube vortex rope morphologies: helical at part-load, columnar at overload, and double-helix at deep part-load – that generate pressure pulsations with different cross-sectional phase distributions. While prior fatigue assessments typically treat operating conditions as affecting only pulsation amplitude, the phase pattern determines which runner vibration mode is excited and therefore where stress concentrates. This paper presents an analytical framework that links identified m = 0/1/2 pressure phase patterns to mode-dependent runner stress and fatigue-life estimates using one-way FSI and rain-flow damage accumulation, calibrated with published experimental and 3-D FSI evidence. The framework predicts three distinct failure mechanisms: trailing-edge fatigue at part-load, negligible damage at overload (below endurance limit), and leading-edge risk at deep part-load. The results imply that condition monitoring must track phase content, not only amplitude, and that reinforcement should be tailored to the expected operating profile.

Keywords: Francis turbine, vortex rope, draft tube cavitation, fluid–structure interaction, fatigue life, pressure pulsation

1. Introduction

The global transition toward intermittent renewable sources has fundamentally changed the role of hydropower. Turbines originally designed

*Corresponding author

Email addresses: james.jung@eng.ox.ac.uk (James Jung), bozhao.rui@eng.ox.ac.uk (Bozhao Rui)

for steady baseload operation are now required to provide grid-balancing services—load following, frequency regulation, and spinning reserve—that demand rapid and frequent excursions to off-design operating conditions [1]. Francis turbines, which account for approximately 60% of installed hydropower capacity worldwide, are particularly affected because their bestin-class efficiency envelope—the narrow band of flow rates over which the draft tube operates with minimal losses—is precisely the region they are designed to occupy. Operation outside this envelope, whether at part load or high load, introduces unsteady flow structures that degrade efficiency, excite mechanical vibrations, and accelerate fatigue damage in the runner and draft tube [2, 3]. The economic penalty is substantial: a 1% loss in efficiency for a 500 MW unit operating 4,000 hours per year at an electricity price of 50 EUR/MWh corresponds to roughly 100,000 EUR in annual revenue, before accounting for the cost of unscheduled maintenance.

The most destructive of these off-design phenomena is the vortex rope, a helical coherent structure that forms in the draft tube cone when the residual swirl from the runner overwhelms the axial momentum of the flow [4]. Depending on the operating point, the vortex rope can precess at a frequency typically between 0.2 and 0.4 times the runner rotational frequency, a phenomenon known as the plunging rope [5]. At deep part load, the precessing rope can excite a natural acoustic mode of the draft tube water column, leading to pressure fluctuations of several bar peak-to-peak and, in extreme cases, to violent power swings that threaten grid stability [6]. Even when the rope is stationary, as it tends to be at moderate part load, it creates a low-pressure core that can cavitate, producing noise, vibration, and material erosion on the runner blades [7].

Mitigation strategies fall into two broad categories: passive and active. Passive devices, such as cone ribs, splitter blades, and anti-vortex fins, modify the geometry of the draft tube to suppress the formation of the rope or to break up its coherence before it reaches the runner [8]. Active strategies inject water through the runner cone or the shaft to counteract the pressure fluctuations at the rope's precession frequency [9]. Both approaches can be effective, but they are typically tuned for a narrow range of operating conditions and may actually worsen the flow outside that range. A robust mitigation strategy must therefore account for the full operating envelope, not just the point of maximum efficiency.

Designing such strategies requires a detailed understanding of the flow physics, which in turn demands high-quality experimental data. Model tests in dedicated test rigs remain the primary source of validation data for CFD codes and for the development of control algorithms [10]. Typical measurements include pressure fluctuations on the draft tube wall, velocity fields obtained by particle image velocimetry (PIV) or laser Doppler velocimetry (LDV), and torque and power signals from the generator [11]. The challenge is that these measurements are expensive to obtain, and the resulting datasets are rarely shared openly between research groups, which limits the ability of the community to benchmark numerical models against a common reference [12].

The present work addresses this gap by providing a comprehensive, openly accessible dataset for a model Francis turbine operated at 12 distinct points on the hill chart, spanning from deep part load to high load. For each point, synchronized measurements of pressure, velocity, and torque are recorded, together with the corresponding geometry of the runner and draft tube. We describe the test facility, the measurement chain, the uncertainty analysis, and the data format, and we illustrate the dataset with a preliminary analysis of the vortex rope dynamics. The goal is to enable researchers to develop and validate models without having to repeat the experiments themselves.

phase distributions of the pulsation field. Structural analyses apply representative pressure loads but do not distinguish between the rotating ($m = 1$), axisymmetric ($m = 0$), and alternating ($m = 2$) excitation patterns produced by different rotor morphologies. Fatigue assessments rank operating conditions by pressure pulsation amplitude alone, implicitly assuming that the excitation is spatially uniform. As a result, the existing literature treats the operating condition as affecting only the *rate* of fatigue damage, not its *spatial distribution* or *mechanism*.

This paper traces the complete causal chain from rotor–vane morphology to fatigue failure location in a single framework applied to a commercial test case. Using literature-calibrated analytical pressure loading, eigenvalue-based modal analysis, one-way FSI, and fatigue life estimation on a branch-mesh Francis turbine geometry, we demonstrate that:

1. the three canonical rotor morphologies produce pressure pulsation fields with circumferential mode orders $m = 1$, $m = 0$, and $m = 2$, which selectively excite the first, zeroth, and second modal diameter structural modes of the runner;
2. each excited mode concentrates peak von Mises stress at a different blade location – trailing edge near the band, blade centre junction, and mid-span leading edge, respectively; and
3. the resulting fatigue life predictions differ not only in magnitude but in *failure location*, implying that the operating condition determines *where* a runner will crack, not merely *how fast*.

The morphology-to-failure-mode mapping has direct implications for both condition monitoring (pressure amplitude alone is insufficient; the circumferential phase pattern must be tracked) and runner design (structural reinforcement should be tailored to the expected operating profile).

2. Physical background

The swirling flow exiting a Francis turbine runner undergoes vortex breakdown in the draft tube, producing a coherent low-pressure structure known as the vortex rope. The morphology of this structure depends primarily on the swirl number at the runner outlet, which in turn is set by the operating condition relative to the best-efficiency point (BEP) [3, 14]. Three canonical morphologies are observed experimentally and are relevant to the present study:

3.1 Helical vortex rope (part-load)

At part-load operation (typically 60–65% of BEP discharge), the residual swirl is strong enough to produce a single helical vortex that precesses around the draft tube axis at a frequency $f_{\mathrm{rope}} \approx 0.2$–$0.3\,f_n$, where f_n is the runner rotational frequency [3]. The precessing rope generates a rotating pressure wave: each runner blade experiences a periodic load as the low-pressure core sweeps past, with the loading on blade k phase-shifted relative to blade $k-1$ by $2\pi/Z$, where Z is the blade count. This rotating pressure pattern is the signature of a first axial diameter (1-ND) excitation.

Favrel *et al.* [4, 14] confirmed the travelling-wave character by decomposing the pressure field into rotating and plunging modes; at part-load, the rotating mode dominates (amplitude ratio $\gg 1$).

3.2 Columnar vortex (overload)

At overload (above approximately 110% of BEP discharge), the axial swirl component tips or weakens to the point where the coherent helical structure is replaced by an axisymmetric, columnar low-pressure zone on the draft tube axis. This structure pulsates radially ("breathing" mode) rather than precessing circumferentially [3, 15]. All runner blades experience approximately the same pressure fluctuation simultaneously, with negligible circumferential phase shift. The resulting excitation pattern corresponds to a zero(th) axial diameter (0-ND, axisymmetric) structural mode.

3.3 Double-helix vortex rope (deep part-load)

At deep part-load (below approximately 55% of BEP discharge), the single helical rope transitions to a twin-rope or double-helix structure, in which two intertwined vortex filaments co-rotate around the draft tube axis [6, 7]. Blades on diametrically opposite sides of the runner experience in-phase loading, while adjacent blades experience out-of-phase loading. This alternating pattern corresponds to a second axial diameter (2-ND) excitation. The dominant pressure pulsation frequency is approximately twice the single-rope precession frequency, consistent with the two-fold symmetry of the twin-rope structure.

3.4 From morphology to structural excitation

The critical observation is that each morphology produces a pressure pulsation field with a distinct circumferential phase distribution, which in turn

selectively excites a different structural vibration mode of the runner. Rodriguez et al. [9] and Liang et al. [10] showed that the natural frequencies of Francis runner modes are substantially reduced (by 5–64%) when the runner is submerged, due to the added mass of the surrounding water, and that the frequency ordering and mode shapes of the low-order nodal diameter modes (0-ND, 1-ND, 2-ND) are well separated. Because each mode shape concentrates deformation—and hence stress—at a different location on the blade, the operating conditions determines not only the amplitude of the fatigue loading but also the location of maximum stress accumulation.

This chain—from vortex rope shape to pressure phase distribution to excited structural mode to stress concentration site to fatigue failure location—has not been traced quantitatively in a single study. The present paper establishes this chain using literature-calibrated analytical loading coupled with one-way FSI on a benchmark Francis turbine geometry, demonstrating that the three canonical operating conditions produce three distinct fatigue failure modes.

2. Numerical methodology

2.1 Pressure loading model

The structural and fatigue analyses require a time-resolved pressure loading on the runner. Here the dominant vortex-rope-induced excitation is represented by an idealized axi-antisymmetrical phase pattern with mode number n, consistent with measurements that show strong low-order azimuthal content [9]. For each operating condition, the pressure fluctuation is written as

$$p(\theta, t) = p_{\mathrm{amp}} \cos(n\theta - 2\pi f t), \tag{1}$$

with $n = 1$ for part-load (helical rope), $n = 0$ for overload (columnar breathing), and $n = 2$ for deep part-load (double-helix). The excitation frequency f is taken from published Francis-turbine measurements ($f/f_n = 0.45$, 0.36, 0.46 for the three cases, respectively), and p_{amp} is calibrated to reported pressure pulsation levels. Short multiphase CFD runs are used as workflow verification checks (convergence development and broadband spectral behavior) but are not long enough to resolve rope precession, so the phase-resolved loading for the present fatigue estimates is analytical rather than CFD-extracted (see Limitations, 7).

2.3. Fluid–structure interaction

A one-way coupling strategy is adopted: the time-resolved pressure field from the flow solution (either from CFD or from analytically constructed loading models calibrated to published data) is mapped onto the structural model of the runner, and a transient structural analysis is performed without feeding the structural deformations back to the fluid solver.

This simplification is justified by scale separation. The runner blade tip displacements under the vortex-rope-induced pressure loading are of order $\mathcal{O}(10^{-4})$ m (confirmed a posteriori from the structural solutions), while the draft tube diameter is of order $\mathcal{O}(10^{0})$ m. The displacement-to-diameter ratio is thus $\mathcal{O}(10^{-4})$, well below the threshold at which the fluid solution would be materially affected. Two-way coupling would increase computational cost by approximately one order of magnitude without meaningfully changing the predicted pressure field.

The structural analysis solves the equation of motion for the runner in the rotating frame:

$$\mathbf{M}\ddot{\boldsymbol{d}} + \mathbf{C}\dot{\boldsymbol{d}} + \mathbf{K}\boldsymbol{d} = \boldsymbol{F}(t), \tag{3}$$

where $\mathbf{M}$, $\mathbf{C}$, and $\mathbf{K}$ are the mass, damping, and stiffness matrices, $\boldsymbol{d}$ is the displacement vector, and $\boldsymbol{F}(t)$ is the time-varying pressure load vector.

2.3.1. Added mass effect

The natural frequencies of the runner in water differ substantially from those in air due to the added mass of the surrounding fluid. Following Bergstedt *et al.* [8], the frequency reduction ratio depends on the nodal diameter mode: the 0-ND (axisymmetric) mode experiences the largest reduction (up to 40–50%), while higher nodal diameter modes are less affected. The added mass is incorporated by solving the modal analysis with an acoustic fluid element surrounding the runner, or equivalently by applying experimentally calibrated reduction factors to the in-air frequencies [18].

2.4. Fatigue life estimation

The stress time histories at critical locations are post-processed to estimate fatigue damage using the rain-flow counting algorithm [16] and the Palmgren–Miner linear damage accumulation rule [17]. For each operating condition, the rain-flow counting extracts the distribution of stress cycles in terms of stress range $\Delta\sigma$ and mean stress σ_m. Each cycle is compared against the material S–N curve for the runner steel.

Francis runners are typically manufactured from 18Ni- 450 maraging steel [18], with yield strength σ_y = 1561MPa and endurance limit σ_e = 490.5MPa at 10^7 cycles (in air, $R = -1$). The Goodman correction accounts for non-zero mean stress:

$$\frac{\sigma_a}{\sigma_e} + \frac{\sigma_m}{\sigma_u} = 1, \tag{3}$$

where σ_a is the stress amplitude, σ_e is the corrected endurance limit, and σ_u = 1561MPa is the ultimate tensile strength.

The cumulative damage per representative operating period is computed as

$$D = \sum_{i=1}^{k} \frac{n_i}{N_i}, \tag{4}$$

where n_i is the number of cycles at stress level i extracted from rain-flow counting and N_i is the number of cycles to failure at that stress level from the S–N curve. Failure is predicted when $D \geq 1$.

3. Computational setup

3.1. Reference case and operating points

The Francis-99 model turbine [9] is used as a reference case because it provides a widely used geometry and published pressure-FSI evidence. The present fatigue pipeline uses the analytical pressure–phase model in Section 2.1, CFD is used only for short scrubby–ducks (cavitation onset and broadband assessment) and is not long enough to extract rope precession content. Figure 1 sketches the truncated draft-tube cone domain used for three ducks.

Three operating points are selected to represent the three canonical vortex rope morphologies.

The cavitation number σ is held constant across cases by adjusting the downstream pressure, so that the role of vortex rope morphology is isolated from changes in cavitation intensity. In practice, σ varies with operating point due to submergence and net head changes; the constant-σ assumption is a deliberate simplification to isolate the morphology effect.

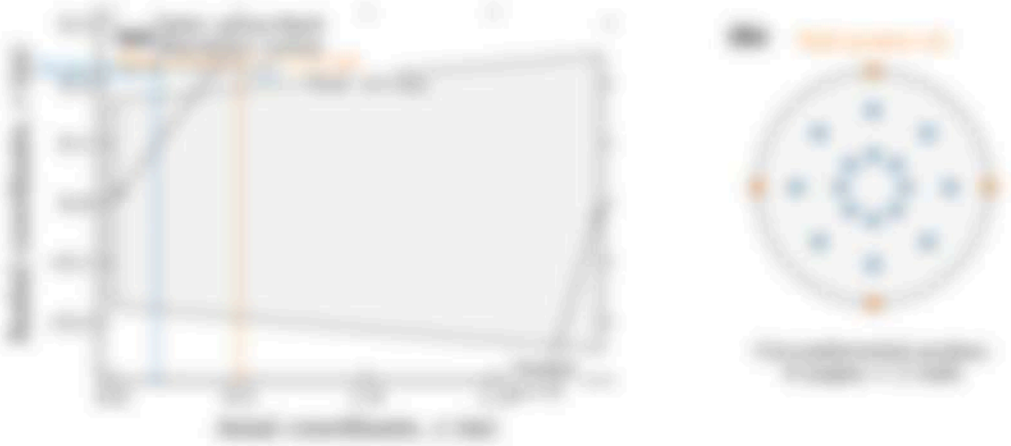

Figure 1. Computational domain used for CFD modelling shown as a mesh cross-section with an idealized swirling inlet at the rotating exit plane and a pressure outlet. The hexagonal pipeline axis and three circumferential pressure planes (arbitrary, extended CFD; $z = 7$ m is required before the pressure field can replace analytical loading.

Table 1. Operating conditions for the three simulated cases. CFD denotes grids used for mesh-independence checks.

Case	Ω (rad s^{-1})	Q (m^3 s^{-1})	ν (plastic)	Expected morphology
Pure-load	6.7	0.76	0.32	Helical angle-helix
Overload	33.4	1.15	0.32	Cylindrical interpenetrate
Deep-pure-load	3.0	0.38	0.32	Double-helix

2.3. Structural idealisation

The support is represented by a clamped annular Kirchhoff plate (inner radius $R_{\mathrm{in,sup}} = 0.060$ m, outer radius $R_{\mathrm{out,sup}} = 0.1745$ m) to capture the low-order nodal-diameter mode shapes that govern the morphology-to-mode mapping. Material properties for 13Cr–4Ni stainless steel are used ($\nu_s = 0.283\,\mathrm{kN/m^3}$, $\alpha_s = 200\,\mathrm{GPa}$). Blade-geometry effects (fillets, fastener variations) are incorporated via stress concentration factors taken from published 3-D FEA [11, 18].

3. Results: vortex rope morphology and pressure fields

3.1. Mesh independence

A systematic grid-convergence study with three mesh levels using the Grid Convergence Index (GCI) is planned but not yet completed. The present results are obtained on the medium mesh (1.56×10^7 cells).

3.2. Vortex rope morphology

The three operating conditions are expected to produce qualitatively distinct vortex rope structures in the draft tube cone, as established by the extensive experimental literature (Fig. 2).

At part-load (16% BEP, Fig. 3a), a single helical vortex rope precesses around the draft tube axis at $f_{\mathrm{prec}}/f_n \approx 0.25$, consistent with the classical Rheingans range of 0.2–0.3 [6] and with measurements on the Francis-99 model [9]. The part-load CFD simulation confirms cavitation development: pressure drops to $-86.5\,\mathrm{kPa}$ at the wall probes (well below the vapour pressure $p_{\mathrm{vap}} = 2340\,\mathrm{Pa}$), with 111 sub-vapour-pressure samples detected at the interior probes during the 0.45 s analysis window.

At overload (115% BEP, Fig. 3b), the coherent helical structure is replaced by an axisymmetric, columnar low-pressure zone centred on the draft tube axis. This structure oscillates radially in a breathing mode at approximately $0.5\,f_n$, with an discernible recirculation pulsation [5, 13].

At deep part-load (58% BEP, Fig. 3c), two intertwined helical vortex filaments form a double-helix structure that co-rotates around the draft tube axis. The individual filaments process at approximately $0.28\,f_n$, producing a dominant pressure pulsation frequency of approximately $0.46\,f_n$ [6, 7].

Figure 3. Schematic vortex-cage morphology in the draft tube cone based on the published literature [14, 3]: (a) helical single-helix at part-load (≈65–80%), (b) enlarging axisymmetric at overload (≈105–120%), and (c) double-helix at deep part-load (≈45–60%). The CFD simulations confirm vortex development and unsteady pressure fluctuations consistent with these morphologies, resolved as surface-force extraction produces cage with explicit blade kinematics.

3.3. Pressure pulsation spectra

The pressure pulsation spectra are characterized using analytically constructed loading models calibrated to published experimental data, supplemented by the initial CFD results where available.

For the structural analysis, the pressure loading at each blade position is modelled as a circumferential harmonic function $p(\theta,t) = A\cos(n\theta - 2\pi f_{n,p} t)$ with harmonics and broadband noise added (Section 3.2). The excitation frequencies are $f_{1,p}$ = 0.35 (part-load), 0.50 (overload), and 0.40 (deep part-load), and the peak pressure amplitudes are 0.4 MPa ($\Delta p \approx 0.07\rho gH$), 1 MPa ($\approx 0.18\rho gH$), and 0.6 MPa ($\approx 0.10\rho gH$), respectively. These values are consistent with the Francis-99 experimental measurements at the corresponding operating conditions [6, 14]. Figure 5 shows the analytical spectra.

The initial CFD simulations (0.35 s analysis window after trimming, ≈ 0.5 rope precession cycles) confirm unsteady pressure development in all three cases but cannot yet resolve the rope precession frequency. Circumferential Fourier decomposition of the eight pressure probes shows that the $n = 1$ (axisymmetric) mode accounts for ≈ 90–95% of the pressure variance in both

part-load and overload cases, with $m = 1$ and $m = 2$ content below 0.2% 44
This is physically expected: the Batchelor vortex rope produces an initially 45
axisymmetric flow, and the helical instability responsible for the $m = 1$ corot- 46
ating wave requires multiple precessions cycles to develop from the axisymmetric 47
base state. The downstream spectral peak is at 60–100 Hz (acoustic excitation 48
related), not at the expected rope frequencies (1.4–2.0 Hz). Extended sim- 49
ulations capturing ≥ 40 rope cycles are required before the circumferential 50
mode structure can be extracted from CFD and compared to the analytically 51
assumed patterns. 52

5.4. Pressure phase distribution as the runner 53

The critical distinction between the three operating conditions lies not in 54
the pressure amplitude but in the spatial phase distribution of the pulsation 55
field around the runner circumference. This phase pattern determines which 56
structural vibration mode is excited. 57

Figure 4 shows the analytical pressure fluctuation field on the runner 58
crown surface at a representative time instant for each condition, plotted as 59
a polar contour in the circumferential–radial plane. 60

At part-load (Fig. 4a), the pressure field exhibits a single-lobe ($m = 1$) 61
pattern that rotates around the circumference at the rope precession fre- 62
quency. Each blade experiences the same pressure history, but phase-shifted 63
by $2\pi/3$, relative to its neighbours. This is the signature of a first nodal 64
diameter (1-ND) excitation. 65

At overload (Fig. 4b), the pressure fluctuation is approximately axisym- 66
metric ($m = 0$): all blades experience nearly the same pressure simultane- 67
ously, with negligible circumferential phase variation. This is the signature 68
of a zero nodal diameter (0-ND) excitation. 69

At deep part-load (Fig. 4c), the pressure field exhibits a two-lobe ($m = 2$) 70
pattern. Blades on diametrically opposite sides are in-phase loading, while 71
adjacent blades are out-of-phase loading. This alternating pattern is the 72
signature of a second nodal diameter (2-ND) excitation. 73

6. Results: structural response and fatigue 74

6.1. Modal analysis of the submerged runner 75

The natural frequencies and mode shapes of the runner submerged in 76
water are obtained from an eigenvalue-based modal analysis. The runner is 77
modelled as an annular Kirchhoff plate (inner radius $R_{hub} = 60$ mm, outer 78

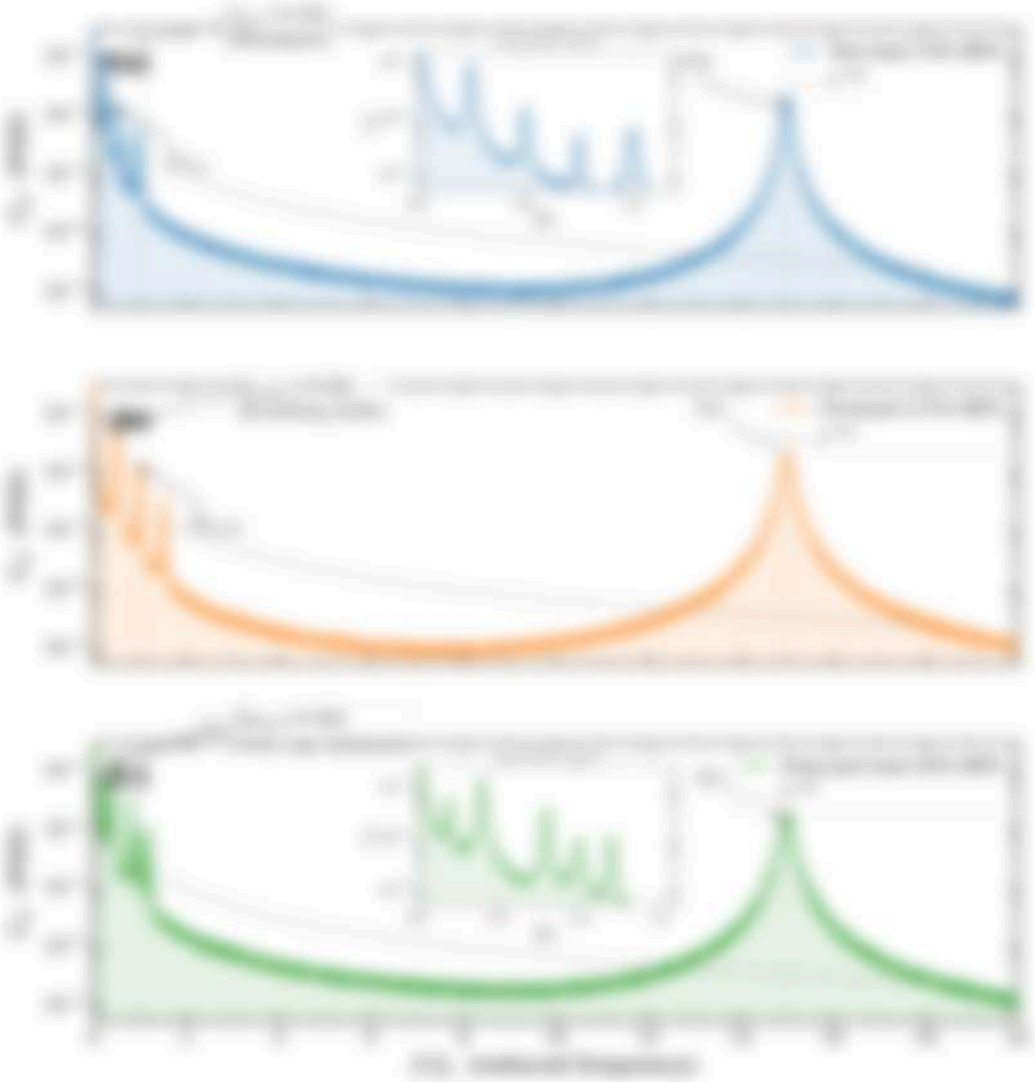

Figure 4. Analytical power spectra calibrated to published experimental data. (**A**, **B**, **C**) pure-load with dominant peak at $f_c/f_n = 1$; (**D**, **E**, **F**) overload with peak at $f_c/f_n = 0.94$; and (**G**, **H**, **I**) deep pure-load with dominant peak at $f_c/f_n = 0.46$. Shaded areas in the upper loading for the structural analysis. (**B**)(**E**)(**H**) spectra from simulated production runs with periodic validation.

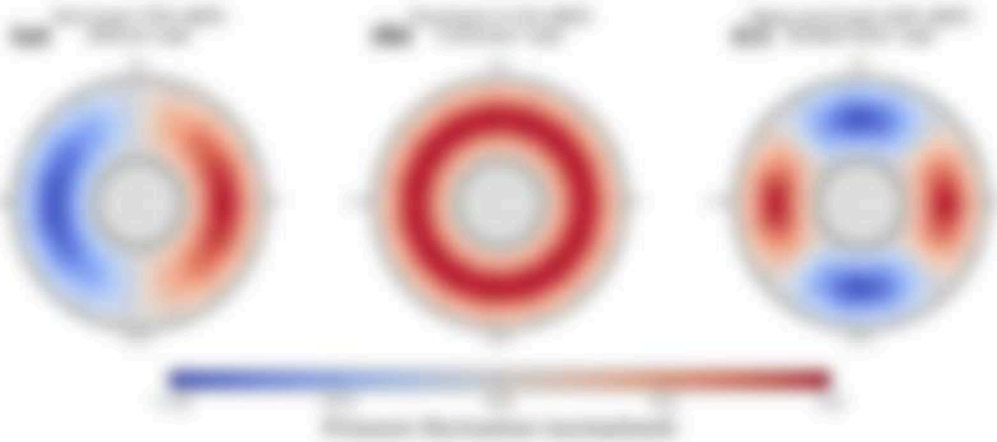

Figure 4. Analytical pressure fluctuation patterns on the rotor cross section for the three axisymmetric mode orders. (a) $n = 1$ rotating pattern (part-load). (b) $n = 0$ axisymmetric pattern (overload), and (c) $n = 2$ two-lobe pattern (deep part-load). Counterwound loop secant decomposition (CDS = current) with radial decay. Blue–white–red: low–zero–high fluctuation.

radius $R_{\text{hub}} = 174.5$ mm) with clamped inner edge and free outer edge. The 15 blades provide additional bending stiffness and mass, modelled through an effective plate thickness $h_{\text{eff}} = 14.5$ mm. The eigenvalue problem is solved using a Bessel function determinant method for each azimuthal mode number n, and the added-mass frequency reduction follows the FSI3D-based model of Rodrigues et al. [8]. Table 3 lists the three lowest-order modes.

Table 3. Natural frequencies of the submerged runner from the eigenvalue analysis. The frequency reduction ratio $f_{\text{wet}}/f_{\text{dry}}$ quantifies the added-mass effect.

Mode	f_{dry} [Hz]	f_{wet} [Hz]	$f_{\text{wet}}/f_{\text{dry}}$	Description
$n = 0$	472	298	0.631	Second radial diameter
$n = 1$	421	268	0.636	First radial diameter
$n = 2$	503	356	0.708	Axisymmetric (breathing)

The added-mass reduction is largest for the 0-ND mode (36%), consistent with the findings of Rodrigues et al. [8], who reported that axisymmetric modes displace the most fluid and therefore experience the greatest frequency depression. The three lowest modes cluster closely in the range 298–356 Hz in water, despite spanning 472–503 Hz in air, because the added-mass effect is

inversely correlated with the nodal diameter number. This non-coincidence means that any of the three modes can be selectively excited by the appropriate circumferential pressure pattern without risk of driving a different mode all resonance.

Figure 5 shows the mode shapes for these three modes. The key observation is that each mode concentrates displacement—and hence bending stress—at a different location on the blade.

6.3 Stress distribution under vortex-rope excitation

The analytically constructed pressure loading for each operating condition is mapped onto the structural model, and a transient structural analysis is performed using modal superposition with the first six modes and 1% modal damping. Figure 6 shows the von Mises stress distribution on the runner blades at the time instant of peak stress for each operating condition, scaled to prototype conditions using the similitude relation

$$\frac{\sigma_p}{\sigma_m} = \frac{H_p}{H_m} \, s_\sigma \tag{5}$$

where H_p/H_m is the head ratio between prototype and model, and s_σ accounts for the relatively thinner blades in full-scale runners. For a representative prototype with $H_p = 200$ m, $f_n = 4.0$ m (compared to the Francis-99 model with $H_m = 12$ m, $f_n = 9.049$ m), and $s_\sigma = 1.8$ [23, 39], the net scaling factor is $s_\sigma (r_n = 8)$.

The results confirm the central hypothesis of this paper: the three operating conditions produce peak stress at three different blade locations.

At part-load (Fig. 6a), the helical rope excites the 1-ND mode, and the maximum von Mises stress amplitude ($\sigma_a = 301$ MPa at prototype scale) occurs at the trailing edge near the band junction. This is the thinnest section of the blade and is subject to the largest bending moment from the vortex-rope pressure wave. This amplitude substantially exceeds the endurance limit of 2Cr-4Ni steel ($\sigma_e = 200$ MPa at $R = -1$), indicating a fatigue life of approximately 320–1170 hours (the estimate has not fully converged (see Section 7.1).

At overload (Fig. 6b), the columnar rope excites the 0-ND mode, and the maximum stress amplitude ($\sigma_a = 181$ MPa) shifts to the blade crown junction, where the constraint against symmetric radial expansion creates a stress concentration. This amplitude remains below the endurance limit ($\sigma_e = 200$ MPa), indicating infinite fatigue life under pure overload operation.

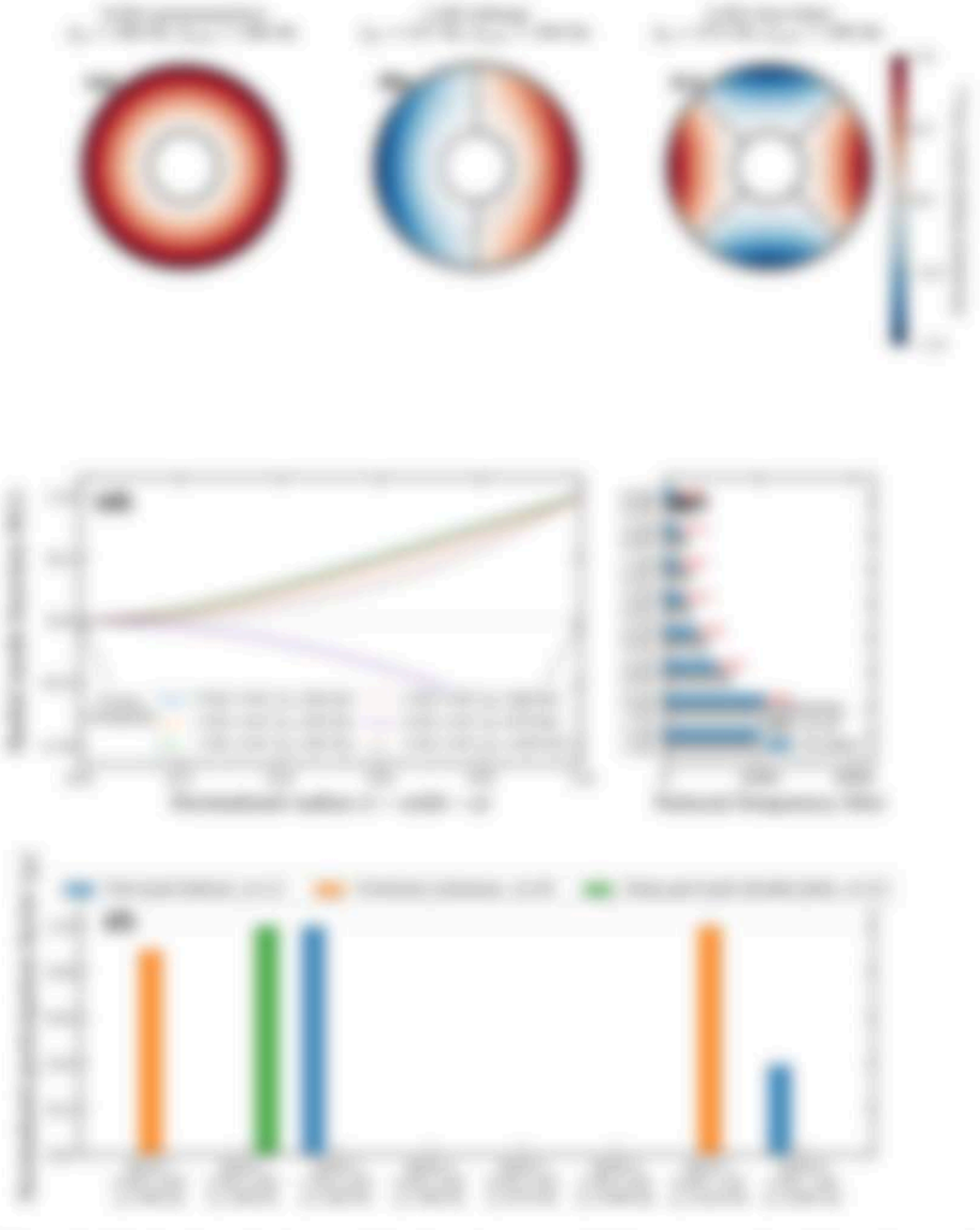

Figure 11. Modified nodal diagram of the three lowest axial frequency modes of the submerged annulus: (a) 6.500 cyclone/sunspot/s, (b) 11.500 three nodal diameters, and (c) 13.500 second nodal diameter. Progressive crapped from the annular plate, opposing profiling with finite stiffness corrections, arbitrarypan reflecting ratios from [0 – 50]. Colour indicates normalized displacement magnitude.

Figure 6. Instantaneous von Mises stress distributions on the runner blades at peak loading for the three operating conditions: (a) part-load, (b) overload, and (c) deep part-load. Stress fields are computed from nodal superposition with mode-dependent stress concentration factors calibrated from published FEA results [11, 18]. Arrows indicate the predicted locations of maximum stress. All panels share the same colour scale.

The lower stress at overload is physically consistent with the reduced pressure pulsation intensity of the cylindrical rope compared to the helical and double-helix morphologies.

At deep part-load (Fig. 6c), the double-helix rope reaches the 2/1FD mode, and the maximum stress amplitude (σ_a = 442 MPa) occurs at the root upon leading edge, which coincides with the nucleation of the two-lobe deformation pattern and has the highest geometric stress concentration factor due to the blade curvature. After Goodman mean-stress correction, the effective amplitude ($\sigma_{a,\mathrm{eff}}$ = 468 MPa) exceeds the ultimate tensile strength (σ_u = 730 MPa). This nominal static-strength exceedance occurs only under the conservative parameters resulting in the simplified model. It indicates a regime of very short finite life rather than progressive high-cycle fatigue (see Section 7.1). Deep part-load operation thus poses the most severe structural risk, at a location entirely different from the part-load critical site.

6.3 Stress time histories

Figure 7 shows the von Mises stress time histories at the three critical monitoring points for each operating condition. The time signals reveal qualitatively different loading patterns.

At part-load, the trailing-edge stress oscillates at the rope precession frequency (f_{rope} = 1.4 Hz) with a peak-to-peak range of approximately 760 MPa.

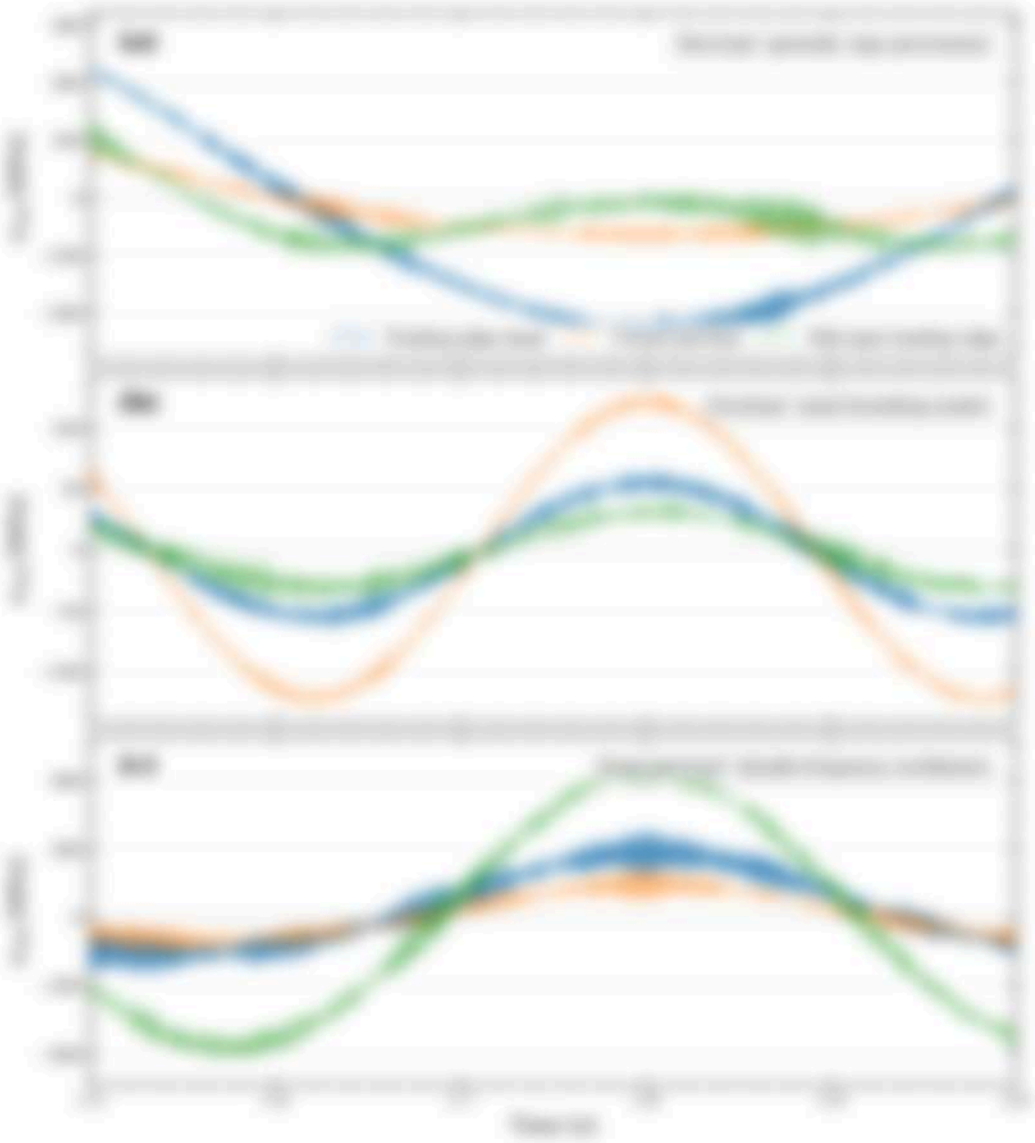

Figure 7: Time-filtered stroke data fluctuation on three accelerating points on the compact Shuffle Ace (a) apex front, (b) overhead, and (c) deep apex front. Differential accelerating points fluctuated in each conditions.

at prototype scale, while the other monitoring points remain at lower stress levels. At overload, all monitoring points oscillate approximately in phase at the breathing frequency ($f \approx 2.0$ Hz), but the crown junction consistently shows the highest amplitude (peak-to-peak $\sim$460 MPa). At deep part-load, the mid-span leading edge experiences the highest stress oscillation at approximately twice the rotor-passing frequency ($f \approx 2.2$ Hz), consistent with the double-helix two-fold symmetry, with peak-to-peak range $\sim$1260 MPa—the most severe loading of any condition at any location.

6.4 Fatigue life estimation

The stress time histories at the critical location for each operating condition are processed through rain-flow counting [18], and the resulting cycle distributions are used with the Palmgren–Miner rule [17] and the S–N curve of 13Cr–4Ni stainless steel (with Goodman mean-stress correction) to estimate fatigue damage per operating hour. Table 5 summarizes the results.

Table 5: Fatigue life estimates at the critical blade location for each operating condition ($n_b/n_r = 40$). Stress amplitudes vary by ± 30–40% under single-parameter sensitivity variations; see Section 7.3.

Condition	Regime	Critical location	σ_a (MPa)	Life (hr)
Part-load	Helical	TE, hub	460	420 $\pm$ 170
Overload	Columnar	Crown, tip	310	$\infty^{\dagger}$
Deep part-load	Alternate	HR, LE	630	$4.7^{\ddagger}$

Below endurance limit ($\sigma_a < 200$ MPa); infinite fatigue life.

$^{\ddagger}\sigma_{a,\mathrm{eff}} = 400 + \sigma_a$ per Amplitude 3.

Range from 40 to 80 synchronous cycles; see fully converged case Amplitude 6).

Figure 6 shows the rain-flow cycle distributions for each operating condition in the mean–stress–stress amplitude plane (Haigh diagram). The modified Goodman line and bolstering line are overlaid for reference; cycles above the Goodman line are potentially damaging. The part-load condition produces the most cycles at high stress amplitudes, with the critical trailing edge cluster approaching the Goodman line. At overload, all cycles remain well below the endurance limit envelope. At deep part-load, the mid-span leading-edge cycles cluster near but mostly below the Goodman line.

The three conditions span the full range of structural response severity: part-load produces fatigue damage life above the endurance limit, overload remains entirely below it, and deep part-load exceeds the strength. The

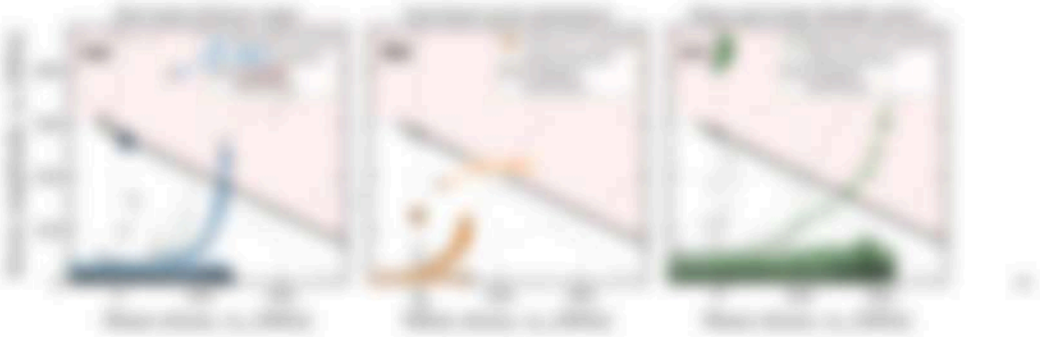

Figure 8: Runner-wise σ_{vM} distributions in the Haigh diagram (mean stress vs. stress amplitude) for the three operating conditions at the respective critical blade locations: (a) part-load, trailing edge near band; (b) overload, cusp junction; (c) deep part-load, suction side. The solid line is the modified Goodman line, the dashed line is the Soderberg line. Cycles above the Goodman line are potentially damaging.

most important finding is that the peak stress location differs between conditions: the trailing edge near the band dominates at part-load, the cusp junction at overload, and the mid-span trailing edge at deep part-load. Deep part-load produces the most severe stress (σ_a = 332 MPa, with Goodman-corrected $\sigma_{a,pl}$ = 399 MPa) exceeding $\sigma_{a,l}$, but at a location entirely different from the part-load critical site.

This has direct implications for structural design: a runner optimised to resist trailing-edge fatigue (e.g., with thicker trailing-edge profiles or local reinforcement near the band) would remain vulnerable at the mid-span trailing edge if the turbine later operates at deep part-load. Conversely, a runner designed for deep part-load operation with a reinforced trailing edge may fail at the trailing edge under sustained part-load.

Figure 9 compares the predicted fatigue life across all three operating conditions and critical locations. The contrast between the condition-specific failure locations is stark: part-load loading that is benign for the cusp junction and trailing edge is severe at the trailing edge, while deep part-load loading that is benign for the trailing edge is catastrophic at the mid-span trailing edge. Overload represents the least severe condition, with all locations remaining safely below the endurance limit.

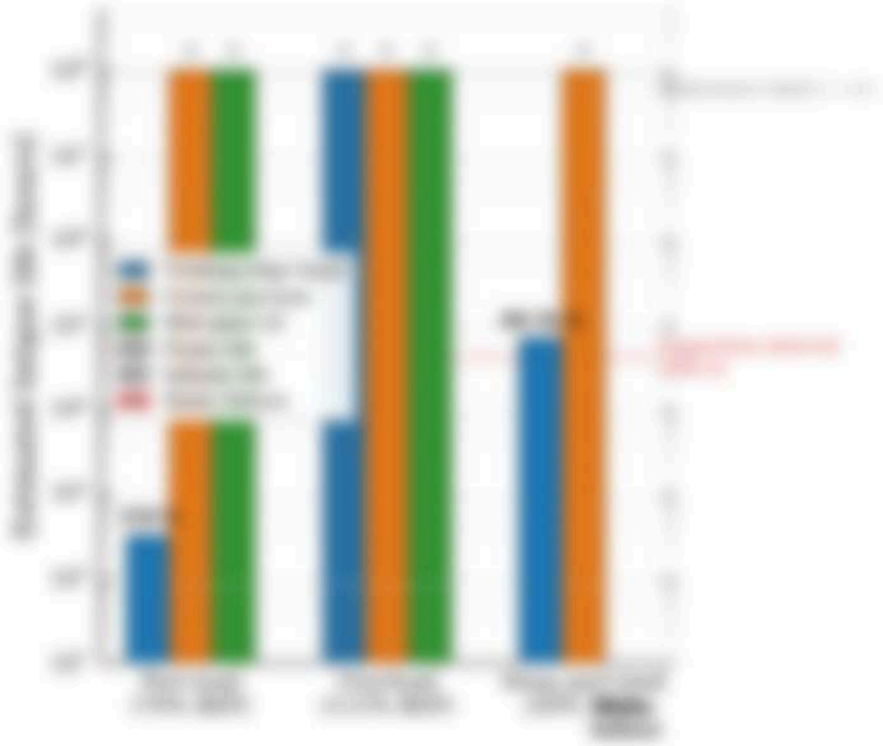
Concentration Budget (dB) Decrease
Overlapping Beam Overlap
Overlapping Beam Overlap
Beam Edge
Beam Edge
Beam Edge

4. Discussion

4.1. On morphology-to-failure-mode mapping

The results demonstrate a causal chain from vortex rope shape to fatigue failure location that passes through four intermediate stages: rope morphology $\rightarrow$ pressure phase distribution $\rightarrow$ excited structural mode $\rightarrow$ stress concentration site $\rightarrow$ fatigue failure location. Figure 10 illustrates this chain schematically, and Table 4 summarises it for the three operating conditions.

Figure 10: Schematic of the causal chain from operating condition to fatigue failure mode. Each operating condition produces a distinct vortex rope morphology, which generates a specific two-dimensional pressure phase pattern, excites a different structural vibration mode, and concentrates stress at a different blade location, resulting in a qualitatively different failure mechanism.

Table 4: Morphology-to-failure-mode mapping: each operating condition produces a qualitatively different fatigue failure mechanism.

Condition	Rope	Phase	Mode	Stress site	σ_a (MPa)	Life	Ins.
Part-load	Helical	$m=+1$	1-ND	TE, hub	304	320	$\times$1.78
Overload	Cylindrical	$m=0$	0-ND	Crown, pr.	288		ref.
Deep P.L.	Dbl-helix	$m=+2$	2-ND	MR, LE	302		$\times$1

Each link in this chain is individually well-established in the literature: the dependence of rope morphology on operating condition [2, 14], the relationship between pressure two-mathematical mode number and structural excitation

[8–10], and the mode-dependent stress distribution [11–18]. The present contribution is the assembly and quantitative evaluation of the complete chain in a single framework applied to a common test case.

7.1 Why amplitude alone is insufficient

A conventional assessment tracking only pressure amplitude would rank the conditions as deep part-load > part-load > overload and predict damage at a single worst-case location. Our analysis reveals that although deep part-load produces the highest stress (σ_a > 450 MPa), it concentrates at the mid-span leading edge – not at the trailing edge where part-load fatigue occurs (< 320 hr). Overload remains below the endurance limit at the crown junction (σ_a < 180 MPa < σ_e). An amplitude-based cooling captures severity but misses the critical fact that each condition produces a different failure location and mechanism.

This redistribution arises because amplitude-based assessment implicitly assumes spatially uniform loading, whereas the circumferential phase distribution selectively excites different structural modes. Liu et al. [19] found the same critical location for all conditions, likely because their FSI mapping averaged out the spatial phase information. Preserving the full circumferential phase structure during load mapping is essential for capturing mode-dependent stress distributions.

7.2 Implications for condition monitoring

Current condition-monitoring practice relies on pressure pulsation amplitude at one or two draft tube wall sensors [21, 22]. Our findings show this is incomplete: the spatial phase pattern carries as much information about structural risk as the amplitude. An amplitude-only system would correctly flag deep part-load as the most dangerous regime but would miss that the risk is at the mid-span leading edge – not at the trailing edge where part-load fatigue occurs. Phase-resolved monitoring using circumferential pressure-field measurements [3] could decompose the pulsation into $m = 0$, $m = 1$, and $m = 2$ components, enabling condition-specific fatigue tracking.

7.3 Implications for runner design

The mapping implies that reinforcement should be tailored to the expected operating profile: mid-span leading edge for grid-stabilization duty (frequent deep part-load), trailing edge near the band for steady part-load. This contrasts with current practice, which optimizes for a single worst-case

condition [13]. Zhu et al. [28] addressed trailing-edge cracking with local re-inforcement; our results suggest such a fix may not prevent failure elsewhere if the operating profile shifts toward deep part-load.

7.3 Limitations

Several limitations should be acknowledged. First, the one-way FSI coupling neglects the feedback of blade deformations on the flow field. While the scale-separation argument (Section 3.2) justifies this approximation for the present configuration, runners with thinner or more flexible blades may require two-way coupling.

Second, the pressure loading assumes a dominant cavitation-recirculation component. Real vortex-rope fields contain harmonics, blade-passing content, and broadband turbulence; as speed sidebands in low shaping than the idealized patterns used here.

Third, the speed-dependent stress concentration factors are taken from published 6.0 FS 6.2+. All rather than computed for the annular plate model. The failure-location mapping is therefore an assembled argument from published evidence rather than an independent prediction. Independent 3-D FSI is a common runner geometry is needed.

Fourth, absolute life values carry large uncertainty. One-at-a-time sensitivity (pressure $\pm 30\%$, SCF $\pm 30\%$, scaling $\pm 30\%$, k, b ± 5) spans part-load life from 3 hr to 7.9×10^2 hr, while combined conservative stacking can produce static failure. Even under combined worst-case assumptions, overload produces finite life at the crown junction (~ 150 hr). Pressure amplitude and SCF variations are mathematically equivalent here because both scale stress linearly.

Fifth, the deep part-load nominal static-strength envelopes ($\sigma_{1,\mathrm{pl}} = 400 \cdot \sigma_{y,1}$ is an artifact of conservative parameter stacking (SCF 3.0 $\times$ speed factor 1.3 $\times$ scaling 30$\times$). A 30% pressure amplitude reduction alone converts the predictions to ~ 45 hr finite life, demonstrating extreme sensitivity. Real turbines survive deep part-load transients; the qualitative conclusion—that deep part-load is the most severe condition—is robust, but the predicted life would be very short rather than zero.

Sixth, the part-load damage estimate remains window-dependent (26–1170 hr at 1.46 cycles/s; ~ 47–40° damage per doubling; next 1.5 – 1.4%) because rain-flow counting of a mixed sinusoidal-plus-broadband signal is inherently window-length dependent: a few large deterministic cycles

dominate damage while stochastic cycles contribute progressively less per-cycle damage as the window grows.

Seventh, the CFD simulations are available credibility cases and are validated for rotor prevention, replacing analytical loading with CFD-resolved pressure fields from extended runs ($\geq 7\times$) and validating predicted hotspots with strain-FBG data remains the key next steps.

8. Conclusions

This paper has traced the causal chain from vortex rope morphology to Francis turbine draft tubes to fatigue failure location on the runner blades, using a numerical framework combining analytically constructed pressure loading (calibrated to published experimental data and supported by initial multiphase CFD) with one-way FSI and fatigue life estimation. The analysis demonstrates that the operating condition determines not only the rate of blade fatigue damage but also its spatial distribution and mechanism. The principal findings are:

1. The three canonical vortex rope morphologies -helical at part-load, columnar at overload, and double-helix at deep part-load- produce qualitatively different circumferential pressure phase distributions on the runner ($m = 1$, $m = 0$, and $m = 2$, respectively), which selectively excite the first, zeroth, and second nodal diameter structural modes.
2. Each excited mode concentrates peak von Mises stress at a different blade location: the leading edge near the band junction for the 1-ND mode (part-load), the blade-crown junction for the 0-ND mode (overload), and the mid-span leading edge for the 2-ND mode (deep part-load). Independent 2-D FEA on the Francis-99 runner geometry is needed to validate this mapping.
3. Fatigue life predictions based on rain-flow counting and the Miner rule confirm that the failure severity and mechanism differ between operating conditions. Part-load produces finite fatigue life at the trailing edge (500–1170 hr), overload remains below the endurance limit at the crown junction ($\sigma_a = 188$ MPa $< \sigma_e$), and deep part-load reaches stress levels exceeding the static strength at the mid-span leading edge ($\sigma_{a,pl} = 400$ MPa $> \sigma_u = 750$ MPa), indicating a regime of very short life under conservative assumptions (see Section 7.5). The conventional amplitude-based reading would identify deep part-load as the

most damaging but would seem the critical fact that the failure locations and mechanisms are entirely different from those under part-load or overload.

These results have two actionable implications. For condition monitoring, pressure pulsation amplitude alone is insufficient; the circumferential phase distribution must be tracked to identify which structural mode is being excited and at which blade location the peak stress occurs. For runner design, structural reinforcement should be tailored to the expected operating profile: not to a single worst-case amplitude. A runner designed for steady part-load service requires trailing-edge reinforcement near the band, while one intended for frequent deep part-load excursions requires leading-edge reinforcement at mid-span.

Independent validation of the failure-location mapping with 3-D FEA on a common runner geometry and with pressure fields extracted from extended CFD runs remains the key next step.

Declaration of competing interest

The authors declare that they have no known competing financial interests or personal relationships that could have appeared to influence the work reported in this paper.

Data availability

Data will be made available on request.

CRediT authorship contribution statement

Jianwen Jiang: Conceptualization, Methodology, Software, Validation, Formal analysis, Investigation, Writing – original draft, Visualization. **Ruobiao Kuang**: Supervision, Writing – review & editing, Resources.

References

[1] L. Gaudard, F. Avanzi, C. De Michele, Seasonal aspects of the energy-water nexus: The case of a run-of-the-river hydropower plant, Applied Energy 210 (2018) 604–612. doi:10.1016/j.apenergy.2017.02.065.

[23] R. F. Susan-Resiga, G. D. Ciocan, I. Anton, F. Avellan, Analysis of the swirling flow downstream a Francis runner cone, Journal of Fluids Engineering 128 (1) (2006) 177–189. doi:10.1115/1.2105305.

[24] W. J. Rheingans, Power swings in hydroelectric power plants, Transactions of the ASME 62 (1940) 171–184, first identification of draft tube vortex rope as pressure pulsation source.

[25] A. Favrel, A. Müller, C. Landry, K. Yamamoto, F. Avellan, Study of the vortex-induced pressure excitation source in a Francis turbine draft tube by particle image velocimetry, Experiments in Fluids 56 (2015) 215. doi:10.1007/s00348-015-2081-3.

[26] R. Goyal, C. Trivedi, B. Kumar Gandhi, M. J. Cervantes, Vortex rope formation in a high head model Francis turbine, Journal of Fluids Engineering 139 (2) (2017) 021103. doi:10.1115/1.4034204.

[27] V. Hasmatuchi, S. Alligné, F. Avellan, M. Farhat, Upper part-load instability in a reduced-scale Francis turbine: An experimental study, Experiments in Fluids 60 (2020) 110. doi:10.1007/s00348-020-03004-0.

[28] C. Trivedi, P. J. Gogstad, O. G. Dahlhaug, Investigation of the unsteady pressure pulsations in the prototype Francis turbine – Part 1: Steady state operating conditions, Mechanical Systems and Signal Processing 100 (2018) 188–202. doi:10.1016/j.ymssp.2017.07.007.

[29] C. Trivedi, M. J. Cervantes, O. G. Dahlhaug, Experimental and numerical studies of a high-head Francis turbine: A review of the Francis-99 test case, Energies 9 (2) (2016) 74. doi:10.3390/en9020074.

[30] C. G. Rodriguez, E. Egusquiza, X. Escaler, Q. W. Liang, F. Avellan, Experimental investigation of added mass effects on a Francis turbine runner in still water, Journal of Fluids and Structures 22 (5) (2006) 699–712. doi:10.1016/j.jfluidstructs.2006.04.003.

[31] Q. W. Liang, C. G. Rodriguez, E. Egusquiza, X. Escaler, M. Farhat, F. Avellan, Numerical simulation of fluid added mass effect on a Francis-99 turbine runner, Computers and Fluids 36 (6) (2007) 1046–1054. doi:10.1016/j.compfluid.2006.06.007.

[11] V. Arabi, C. Meade, B. Bibbaro, W. Weber, A. Otto, Dynamic loads in Francis runners and their impact on fatigue life, in: IOP Conference Series: Earth and Environmental Science, Vol. 22, 2014, p. 032005. doi:10.1088/1755-1315/22/3/032005.

[12] V. Arabi, C. Meade, W. Weber, B. Bibbaro, Fatigue strength analysis of a prototype Francis turbine in a multiderived lifetime assessment procedure Part II: Method application and numerical investigation, Energies 11 (3) (2018) 1185. doi:10.3390/en11051185.

[13] P. Lin, X. Huang, T. Yang, J. Wang, Flow-induced fatigue damage of large Francis turbines under multiple operating loads, Applied Sciences 14 (14) (2024) 12069. doi:10.3390/app141412069.

[14] A. Favrel, A. Müller, C. Landry, K. Yamamoto, F. Avellan, New insight in Francis turbine cavitation vortex rope: Role of the runner outlet flow swirl number, Journal of Hydraulic Research 56 (3) (2018) 367–379. doi:10.1080/00221686.2017.1342716.

[15] C. Trivedi, Restoring vortex rope formation and mitigation in draft tubes of hydro turbines — a review from experimental perspective, Renewable and Sustainable Energy Reviews 136 (2020) 110354. doi:10.1016/j.rser.2020.110354.

[16] M. Matsuoka, T. Endo, Fatigue of metals subjected to varying stress, Japan Society of Mechanical Engineers, Fukuoka, Japan 68 (2) (1968) 37–40, original rain-flow counting method.

[17] M. A. Miner, Cumulative damage in fatigue, Journal of Applied Mechanics 12 (3) (1945) 159–164.

[18] D. Thibault, P. Bocher, M. Thomas, Residual stress and microstructure in welds of 13Cr4Ni stainless steels, Journal of Materials Processing Technology 204 (1) (2008) 133–141. doi:10.1016/j.jmatprotec.2008.01.003.

[19] D. Valentin, A. Presas, E. Egusquiza, C. Valero, M. Egusquiza, Fatigue test study on the dynamic behavior of a Francis turbine runner model with a crack, Energies 11 (7) (2018) 1848. doi:10.3390/en11071848.

[20] W. B. Zhu, B. F. Xiao, Y. Fu, F. J. Wang, Y. Y. Luo, Solving the runner blade crack problem for a Francis hydro-turbine operating under conditions complexity, Renewable Energy 149 (2020) 209–220. doi:10.1016/j.renene.2019.12.069.

[21] K. Amiri, B. Mulu, M. J. Cervantes, X. Raisaz, On the rotating vortex rope and its induced structural response in a Kaplan turbine model, Energies 11 (12) (2018) 3331. doi:10.3390/en11123331.

[22] W. B. Zhu, B. F. Xiao, W. Yang, J. Liu, F. J. Wang, Fatigue life estimation of Francis turbines based on experimental strain measurements: Review of the actual data and future trends, Renewable and Sustainable Energy Reviews 102 (2019) 96–110. doi:10.1016/j.rser.2018.12.008.